Title: Direct observation of 2D magnons in atomically thin CrI_3

Authors: John Cenker[1†], Bevin Huang[1†], Nishchay Suri[2], Pearl Thijssen[1], Aaron Miller[1], Tiancheng Song[1], Takashi Taniguchi[3], Kenji Watanabe[3], Michael A. McGuire[4], Di Xiao[2]*, Xiaodong Xu[1,5]*

[1]Department of Physics, University of Washington, Seattle, Washington 98195, USA
[2]Department of Physics, Carnegie Mellon University, Pittsburgh, Pennsylvania 15213, USA
[3]National Institute for Materials Science, 1-1 Namiki, Tsukuba 305-0044, Japan
[4]Materials Science and Technology Division, Oak Ridge National Laboratory, Oak Ridge, Tennessee 37831, USA
[5]Department of Materials Science and Engineering, University of Washington, Seattle, Washington 98195, USA

[†]These authors contributed equally to this work.

*Corresponding author's e-mail: xuxd@uw.edu; dixiao@cmu.edu

Abstract: Magnons are collective spin excitations in crystals with long-range magnetic order. The emergent van der Waals magnets[1–3] provide a highly tunable platform to explore magnetic excitations in the two-dimensional (2D) limit with intriguing properties, manifesting from their honeycomb lattice structure and switchable magnetic configurations. Here, we report the direct observation of 2D magnons through magneto-Raman spectroscopy with optical selection rules determined by the interplay between crystal symmetry, layer number, and magnetic states in atomically thin CrI_3. In monolayers, we observe an acoustic magnon mode at ~0.3 meV. It has strict cross-circularly polarized selection rules locked to the magnetization direction that originates from the conservation of angular momentum of photons and magnons dictated by threefold rotational symmetry[4]. Additionally, we reveal optical magnon modes at ~17 meV. This mode is Raman-silent in monolayers, but optically active in bilayers and bulk due to a relaxation of the parity criterion resulting from the layer index. In the layered antiferromagnetic states, we directly resolve two degenerate optical magnon modes with opposite angular momentum and conjugate optical selection rules. From these measurements, we quantitatively extract the spin wave gap, magnetic anisotropy, intralayer and interlayer exchange constants, and establish 2D magnets as a new platform for exploring magnon physics.

Main Text:

Symmetry plays a foundational role in determining the characteristics of a physical system. Due to their reduced dimensionality, atomically thin van der Waals materials provide a natural platform to realize the symmetry tuning and consequent control of various quantum phenomena. In layered 2D magnets, magnetic order contributes an additional degree of freedom in symmetry tuning. One example is bilayer CrI_3, which possesses a centrosymmetric crystal lattice. Below its magnetic ordering temperature, two individual ferromagnetic (FM) monolayers are antiferromagnetically (AFM) coupled[1,5–7]. This layered AFM configuration breaks inversion symmetry. When a magnetic field of ~0.7 T is applied, a metamagnetic transition occurs that leads to an FM-like state with restored inversion symmetry. Switching between these magnetic states provides direct control over the symmetry of the bilayer, leading to giant second-harmonic generation[8] and tuning of inelastic light scattering from spin-coupled phonons[9,10]. Changes in symmetry may also affect the magnetic excitations, *i.e.* magnons, in these atomically thin magnets[7,11–14]. While Raman studies have revealed spin wave features in samples as thin as eight layers[15,16], detection of magnons in the atomically thin limit, and thus the study of the impact of the symmetry on magnon physics, remains elusive.

In order to investigate the effects of symmetry on magnetic excitations, we performed magneto-Raman measurements on encapsulated monolayer and bilayer CrI_3 flakes. We utilized a HeNe laser with a wavelength of 632.8 nm which is nearly resonant with a ligand-to-metal charge transfer transition at 2 eV (see Methods)[17]. All measurements were done in the backscattering geometry where both the incident and scattered light are normal to the sample plane. We start by looking at magnons in CrI_3 monolayers. With two Cr^{3+} ions per unit cell, two branches of spin waves are expected, corresponding to an acoustic mode with in-phase precession (Fig. 1a) and an optical mode with out-of-phase precession (Fig. 1b)[18–20]. The spin wave gap, determined by the strong magnetic anisotropy, is theoretically predicted to be around 0.3 to 0.4 meV (2.4 – 3.2 cm^{-1})[21,22], which is in principle accessible by Raman spectroscopy measurements. The magnetic behavior of these samples was confirmed through polar reflective magnetic circular dichroism (RMCD) measurements in the same setup. A representative CrI_3 monolayer is shown in Fig. 1c (optical micrograph, left inset). The zero-field RMCD mapping and RMCD sweep versus magnetic field (right inset) confirms that the flake is a hard ferromagnet with a single domain.

Figure 1d shows the cross-circularly polarized low-frequency Raman spectra of monolayer CrI_3 at select magnetic fields (see Figure S1 for full Raman spectra including co-circular channels). To suppress the strong laser scattering, we used an optical filter with a cutoff near ±3 cm^{-1} (see Methods), indicated by the gray shaded box. At zero field, the spectra are dominated by leakage of the Rayleigh scattered light. When a magnetic field is applied, a low-frequency feature emerges in only the cross-circularly polarized channel (Figs. 1e&f, see Fig. S1 for co-polarized spectra). The low-frequency mode appears on both Stokes and anti-Stokes sides, which are labeled as AM and AM*, respectively. These Stokes and anti-Stokes modes obey distinctly opposite optical selection rules: for a given magnetization orientation, AM only appears when excited by one helicity of light, while AM* emerges with excitation of the opposite helicity. For instance, with the magnetization pointing down (Fig. 1e), only σ^+ excitation can create the AM mode with nearly perfect σ^- polarization (σ^+/σ^-), while the σ^+ polarized AM* mode is excited by σ^- polarized light (σ^-/σ^+). When the direction of the magnetization is flipped, the selection rules correspondingly reverse, as seen in Fig. 1f.

Figure 2a shows the intensity plot of AM and AM* as a function of Raman shift and magnetic field. The extracted peak positions at each field are plotted in Fig. 2b. Both Stokes and anti-Stokes peaks shift linearly with applied field at a slope of 0.94 cm^{-1}/T (.12 meV/T). This is consistent with the Zeeman energy shift of a spin-1 quasiparticle with a magnetic moment of 2 μ_B, the signature of a magnon. Extrapolating the magnon energy to zero field yields the spin wave gap, which we determine to be ~2.4 cm^{-1} (or ~0.3 meV) in monolayer CrI_3. This spin wave gap is quite large for a ferromagnet due to the large magnetic anisotropy and is in excellent agreement with the theoretical predictions in refs. [21] and [22]. We note that the monolayer spin wave gap is also consistent with the results from Raman measurements on bulk single crystal CrI_3 (see Figure S2). This implies that the acoustic magnon properties are determined mainly by out-of-plane magnetic anisotropy.

Temperature-dependent measurements further confirm the magnetic origin of AM and AM*. Figure 2c shows the AM and AM* intensity plotted as a function of temperature and Raman shift. The applied magnetic field is kept fixed at -7 T, thereby shifting the magnon mode away from the Rayleigh scatter and stabilizing the spin-polarized state at higher temperatures. This allows for the study of the acoustic magnon through a wide temperature range. The magnon feature persists and slightly redshifts until temperatures as high as 80 K at which point the scattering becomes too weak to detect. It is worth noting that the linewidth remains essentially constant through the whole temperature range (see Fig. S3 for Raman spectra at select temperatures). This implies that the true linewidth, Γ, is limited by the resolution of our spectrometer. As a result, we infer a lower bound of the lifetime, τ, as Γ^{-1} = 5 ps. These results call for further ultrafast time-resolved measurements in order to determine the true magnon lifetime and its dependence on temperature and magnetic field.

The distinct cross-circular optical selection rules can be derived by considering the angular momentum of the photon, J_p, magnon, J_m in a honeycomb lattice (Fig. 2d). For instance, when the magnetization points up, the total change of photon angular momentum is $\Delta J_p = \pm 2\hbar$ since the helicities between incident and scattered light are opposite, where + (−) corresponds to anti-Stokes (Stokes) scattering from the magnon mode. The change of magnon angular momentum contributes $\Delta J_m = \pm\hbar$. This leads to a total change of angular momentum that is $\Delta J_p + \Delta J_m = \pm 3\hbar$. In a system with continuous rotational symmetry, the conservation of angular momentum would forbid such a process. However, in an analogue to the Umklapp process[4,23], the threefold symmetry of the honeycomb lattice in monolayer CrI_3 allows for discrete angular momentum conservation up to modulo $3\hbar$: $|\Delta J_p + \Delta J_m|/\hbar = 0 \pmod 3$. Given that the total change of the angular momentum is a multiple of $3\hbar$, cross-circular selection rules are expected in monolayer CrI_3. A group theory analysis yields the same conclusion (see Methods). We note that for bulk single crystals (Figure S2), we observe a relaxation of this selection rule. The magnon scattering is still predominately in the cross-circular channels, but significant scattering in the co-circular channels is also present. This deviation from the expected selection rules could potentially originate from stacking faults and highlights the intriguing physics afforded by studying atomically thin samples with pristine crystal structures.

Unlike the monolayer, bilayer CrI_3 hosts either a ferromagnetic-like state or a layered antiferromagnetic state, depending on the applied magnetic field, below a critical temperature of 45 K. Figure 3a shows the low-frequency Raman spectrum of a CrI_3 bilayer in an applied field of 6 T. Since the magnetization of both layers are aligned in the same direction by the magnetic field,

the bilayer essentially behaves like a ferromagnetic monolayer. That is, the acoustic magnon mode is cross-circularly polarized with the Stokes and anti-Stokes peaks showing opposite selection rules and shifts linearly in energy with a g factor of ~2.1 under applied field (Fig. 3b). However, in contrast to the monolayer, we observe switching of acoustic magnon modes as the bilayer undergoes a metamagnetic transition between -0.7 T and -0.75 T (see Fig. S4 for RMCD measurements with consistent transition field). Figure 3c shows a series of Raman spectra as the magnetic states switch from the AFM to the FM-like state. Since the shift of the magnon peak over small field ranges near the metamagnetic transition is smaller than the resolution of our spectrometer, we utilize Lorentzian fits to track subtle changes in the magnon energy (see Fig. S5). In the AFM state, at fields close to the metamagnetic transition, the acoustic magnon mode has a frequency of ~3.6 cm^{-1}. As the field passes the metamagnetic transition, the magnon mode at 3.6 cm^{-1} vanishes. Instead, another acoustic mode, starting at a lower frequency of ~3.0 cm^{-1}, appears and linearly shifts to higher energy as the magnitude of the field increases.

The zero-field magnon energy of the antiferromagnetic acoustic magnon mode, which we find to be ~0.37 meV from a linear fit (green line in Fig. 3b), is given by $\sqrt{(2J_{\mathrm{inter}} + K)K}$, where J_{inter} is the antiferromagnetic interlayer exchange interaction, and K is the magnetic anisotropy[24]. We can extract the magnetic anisotropy by extrapolating the linear fit (blue line, Fig. 3b) of the acoustic magnon energy shift in the FM-like state to zero field. Doing so results in K ~ 0.27 meV which allows us to find J_{inter} ~ 0.11 meV. Therefore, bilayer CrI_3 is in the weak exchange limit ($K > J_{\mathrm{inter}}$). As the magnetic field increases, instead of a spin-flop transition, bilayer CrI_3 undergoes an abrupt spin-flip transition[1,20], explaining the observed discontinuity of the magnon frequency at the spin-flip field. The weak interlayer exchange J_{inter} also explains why the cross-circular optical selection rules continue to hold for bilayer CrI_3 even though the crystal structure lacks three-fold rotational symmetry due to its monoclinic stacking[8,25–28].

In addition to the low-frequency acoustic magnons, we also resolve a high-frequency cross-polarized mode in bilayers which has not been observed in previous Raman studies on CrI_3. Figure 4a shows a very weak and broad peak centered at ~148 cm^{-1} (4.4 THz or 18.4 meV) at 8 T which exhibits the same helicity-dependent selection rules as the acoustic magnon mode. Magnetic field-dependent measurements show that the peak position shifts linearly with a g factor of ~2 (Fig. 4b). Consequently, we assign this peak as the high-frequency optical magnon (OM). This is in sharp contrast to monolayers where the optical mode is Raman silent. As illustrated in Fig. 4c, the optical magnon mode does not show up in monolayers because it has the form $S_A^- - S_B^-$, where S_A^- and S_B^- are the spin wave basis on the two different sublattices in the unit cell. This excitation is thus parity-odd and Raman-silent. In bilayers, the optical modes from both layers will hybridize, leading to a Davydov-like splitting, with one mode being parity-odd and the other parity-even and consequently Raman-active (Figs. 4d&e, see Methods). This optical magnon mode is related to the intralayer exchange by $E = K + 6J_{\mathrm{intra}}$. Therefore, we determine the intralayer exchange to be ~2.83 meV. We also observed the terahertz optical magnon in both exfoliated thin bulk and unexfoliated single crystal samples (see Fig. S6) with frequencies of 160 cm^{-1} (4.8 THz or 19.8 meV) and 148 cm^{-1} (4.4 THz or 18.4 meV) respectively. We note that the optical magnon energy is consistent with that seen in recent neutron scattering experiments[18].

Unlike the low-frequency acoustic magnon which merges with Rayleigh scatter, we are able to resolve the OM mode down to zero applied field and observe its behavior in the AFM state. In

stark contrast to the FM-like state, the OM mode in the AFM state can be excited by both helicities of incident light, giving equal scattering intensity in both σ^+/σ^- and σ^-/σ^+ detection channels in the absence of applied field (Fig. 4f). Applying a small field of 0.5 T, however, results in an energy splitting between the OM features seen in the two cross-circular channels shown in Fig. 4g: the OM mode in the σ^-/σ^+ channel blueshifts while the peak in the σ^+/σ^- channel redshifts. Flipping the direction of the applied field to -0.5 T in Fig. 4h reverses the splitting such that the OM mode in the σ^+/σ^- (σ^-/σ^+) channel is at a higher (lower) frequency.

In general, antiferromagnets with easy axis anisotropy, such as bilayer CrI_3, host two magnon modes per branch which are degenerate at zero-field but carry opposite angular momentum[24,29]. The layered antiferromagnetic order breaks inversion symmetry, eliminating the parity criterion and hence allowing Raman activity of both optical magnon modes. Upon the application of a magnetic field, the two modes shift oppositely, *i.e.* one mode will blueshift and the other will redshift. This explains the Raman activity of the optical branch magnons in both cross-circular channels and the opposite energy splitting of the two OM modes in Figs. 4g&h. The acoustic branch magnons also split in an applied magnetic field, but the redshifted magnon mode (denoted by the orange line in Fig. 3b) is overshadowed by Rayleigh scatter, making it unresolvable in our measurements.

In conclusion, we have identified acoustic and optical magnons in atomically thin CrI_3 which obey selection rules dictated by discrete angular momentum conservation in a honeycomb lattice. Using the energies of the acoustic magnons, we calculate the strength of anisotropy and interlayer exchange. The optical magnon, on the other hand, allows for the determination of intralayer exchange. Furthermore, in contrast to the low-frequency acoustic magnons and those observed in standard FM spintronic systems, the frequency of the optical magnon is well into the terahertz regime and is comparable to those found in AFM systems[30]. As CrI_3 is an insulator, the lifetime of terahertz magnons may be much longer than those in metallic systems[31,32]. Indeed, we determine that the lifetime is on the order of picoseconds, an order of magnitude longer than those seen in recent high-quality metallic FM thin films[32,33]. Our results establish CrI_3 as a desirable candidate for studying fundamental magnon physics with symmetry control and exploring magnonic devices in both the gigahertz and terahertz regime.

Note: We note that while preparing this manuscript, we became aware of similar work on magnons in few-layer CrI_3[35].

Methods

Sample Preparation:

Bulk CrI_3 crystals were grown by direct vapor transport and exfoliated onto 90 nm SiO_2/Si substrates. Using the optical contrast between the flakes and the substrate, monolayer and bilayer flakes of CrI_3 were identified and encapsulated between two 20-30 nm thick hexagonal boron nitride (hBN) flakes. All steps of the fabrication process were performed in a glovebox with N_2 atmosphere.

Encapsulated samples were assembled through a dry transfer technique with a stamp consisting of a poly(bisphenol A carbonate) (PC) film stretched over a polydimethylsiloxane (PDMS)

cylinder[34]. The flakes were picked up in the following order before being deposited onto the SiO_2/Si substrate: top hBN, CrI_3, bottom hBN.

Optical Measurements:

RMCD measurements of CrI_3 samples were performed in a cold finger cryostat capable of reaching temperatures down to 15 K and applying magnetic fields up to 7 T. Raman measurements of the acoustic magnon mode and of the optical magnon mode in single crystal bulk and exfoliated thin bulk CrI_3 were performed in the same setup. Raman measurements of the optical magnon mode in bilayer CrI_3 were taken in an attoDry 2100 cryostat utilizing helium as the exchange gas, allowing the sample to be cooled to 1.6 K and the application of magnetic fields up to 9 T. Unless stated otherwise, the sample temperature was 15 K for all measurements except the optical magnon mode in bilayers (Fig. 4) which had a sample temperature of 1.6 K.

For both RMCD and Raman measurements, an objective lens was used to focus 632.8 nm light from a HeNe laser to a beam spot of ~1.5 μm in the backscattering geometry. Various laser powers were used for the different samples in order to prevent degradation: monolayer and bilayer measurements of the acoustic magnon utilized 400 μW of power with an integration time of two minutes, bilayer and single crystal bulk measurements of the optical magnon used 1 mW of power and five-minute integrations, and measurements of exfoliated thin bulk CrI_3 used 1.5 mW of power with one-minute integrations. There is no laser heating of the samples as a result of using high fluences. The scattered light was collected and dispersed by either an 1800 or 1200 mm^{-1} groove density grating for low-frequency and high-frequency measurements respectively. BragGrate™ notch filters were utilized to reject Rayleigh scattering and enable the study of Raman features down to ~ ±3 cm^{-1} where + (-) corresponds to the Stokes (anti-Stokes) side.

Symmetry analysis of the Raman tensor:

In monolayer CrI_3, the Cr^{3+} ions form a honeycomb structure with two inequivalent sites (denoted by *A* and *B*) per unit cell. Consequently, the magnon spectrum has two branches, which we call the acoustic and optical branches following the convention for phonons. The magnetic point group of monolayer CrI_3 is $D_{3d}(C_{3i}) = C_{3i} + \theta c_{2x} C_{3i}$, where θ is the time reversal operator. In the Hermann–Mauguin notation, the magnetic point group is denoted by $\bar{3}m'$. Since the system has inversion symmetry, the magnon modes at the Γ point are eigenmodes of the parity operator. Specifically, the acoustic mode is given by $S_a = S_A + S_B$ and the optical mode by $S_o = S_A - S_B$. The inversion operation switches the *A* and *B* sites but leaves spin invariant. Therefore, the optical mode (S_o) is parity-odd and hence Raman-silent. On the other hand, the acoustic mode (S_a) is parity-even and Raman-active. To determine the Raman tensor for the acoustic mode, we note that S_a^x and S_a^y transform according to the E_g irreducible representation of $\bar{3}m'$. As a result, the polarizability tensor has the following expansion in terms of the spin wave basis:

$$\alpha = \begin{pmatrix} iA & -A & B \\ -A & -iA & -iB \\ B & -iB & 0 \end{pmatrix} S_a^+ + \begin{pmatrix} iC & C & D \\ C & -iC & iD \\ D & iD & 0 \end{pmatrix} S_a^-,$$

where $S_a^{\pm} = S_a^x \pm iS_a^y$. These two terms are the contributions from the anti-Stokes and Stokes modes. One can see that these two modes satisfy opposite cross-circularly polarized optical selection rules.

We now consider the FM-like state of bilayer CrI_3. In this case, inversion remains a symmetry of the system and we can continue using parity to classify the magnon modes. The magnon modes from the top and bottom layer will hybridize due to the interlayer exchange, giving rise to a Davydov-like splitting. The two optical modes are given by $S_o^- = (S_{A1}^- - S_{B1}^-) \pm (S_{A2}^- - S_{B2}^-)$, where $A1$ denotes the A site in layer 1. One of the modes is parity-odd and thus Raman-silent, while the other is parity-even and Raman-active.

Data Availability: The datasets generated during and/or analysed during this study are available from the corresponding author upon reasonable request.

References:

1. Huang, B. *et al.* Layer-dependent ferromagnetism in a van der Waals crystal down to the monolayer limit. *Nature* **546**, 270–273 (2017).
2. Gong, C. *et al.* Discovery of intrinsic ferromagnetism in two-dimensional van der Waals crystals. *Nature* **546**, 265-269 (2017).
3. Lee, J. U. *et al.* Ising-Type Magnetic Ordering in Atomically Thin $FePS_3$. *Nano Lett.* **16**, 7433–7438 (2016).
4. Higuchi, T., Kanda, N., Tamaru, H. & Kuwata-Gonokami, M. Selection rules for light-induced magnetization of a crystal with threefold symmetry: The case of antiferromagnetic NiO. *Phys. Rev. Lett.* **106**, 047401 (2011).
5. Thiel, L. *et al.* Probing magnetism in 2D materials at the nanoscale with single-spin microscopy. *Science* **364**, 973-976 (2019).
6. Song, T. *et al.* Giant tunneling magnetoresistance in spin-filter van der Waals heterostructures. *Science* **360**, 1214-1218 (2018).
7. Klein, D. R. *et al.* Probing magnetism in 2D van der Waals crystalline insulators via electron tunneling. *Science* **360**, 1218–1222 (2018).
8. Sun, Z. *et al.* Giant nonreciprocal second-harmonic generation from antiferromagnetic bilayer CrI_3. *Nature* **572**, 497–501 (2019).
9. Huang, B. *et al.* Tuning inelastic light scattering via symmetry control in the two-dimensional magnet CrI_3. *Nat. Nanotechnol.* **15,** 212–216 (2020).
10. Zhang, Y. *et al.* Magnetic Order-Induced Polarization Anomaly of Raman Scattering in 2D Magnet CrI_3. *Nano Lett.* **20**, 729–734 (2020).
11. MacNeill, D. *et al.* Gigahertz Frequency Antiferromagnetic Resonance and Strong Magnon-Magnon Coupling in the Layered Crystal $CrCl_3$. *Phys. Rev. Lett.* **123**, 047204 (2019).
12. Kapoor, L. N. *et al.* Evidence of standing spin-waves in a van der Waals magnetic material. *Preprint at: https://arxiv.org/abs/2001.05981.*
13. Xing, W. *et al.* Magnon Transport in Quasi-Two-Dimensional van der Waals Antiferromagnets. *Phys. Rev. X* **9**, 011026 (2019).
14. Costa, A. T., Santos, D. L. R., Peres, N. M. R. & Fernández-Rossier, J. Topological magnons in CrI_3 monolayers: an itinerant fermion description. *Preprint at: https//arxiv.org/abs/2002.00077*.

15. Li, S. *et al.* Magnetic field-induced quantum phase transitions in a van der Waals magnet. *Phys. Rev. X* **10**, 011075 (2020).
16. McCreary, A. *et al.* Distinct magneto-Raman signatures of spin-flip phase transitions in CrI_3. *Preprint at: https://arxiv.org/abs/1910.01237*.
17. Seyler, K. L. *et al.* Ligand-field helical luminescence in a 2D ferromagnetic insulator. *Nat. Phys.* **14**, 277–281 (2018).
18. Chen, L. *et al.* Topological Spin Excitations in Honeycomb Ferromagnet CrI_3. *Phys. Rev. X* **8**, 041028 (2018).
19. Jin, W. *et al.* Raman fingerprint of two terahertz spin wave branches in a two-dimensional honeycomb Ising ferromagnet. *Nat. Commun.* **9**, 5122 (2018).
20. H. H. Kim, *et al.* Evolution of interlayer and intralayer magnetism in three atomically thin chromium trihalides. *Proc. Natl. Acad. Sci. U.S.A.* **116**, 11131–11136 (2019).
21. Lado, J. L. & Fernández-Rossier, J. On the origin of magnetic anisotropy in two dimensional CrI_3. *2D Mater.* **4**, 035002 (2017).
22. Lee, I. *et al.* Fundamental Spin Interactions Underlying the Magnetic Anisotropy in the Kitaev Ferromagnet CrI_3. *Phys. Rev. Lett.* **124**, 017201 (2020).
23. Hisatomi, R. *et al.* Helicity-Changing Brillouin Light Scattering by Magnons in a Ferromagnetic Crystal. *Phys. Rev. Lett.* **123**, 207401 (2019).
24. Keffer, F. & Kittel, C. Theory of antiferromagnetic resonance. *Phys. Rev.* **85**, 329 (1952).
25. Ubrig, N. *et al.* Low-temperature monoclinic layer stacking in atomically thin CrI_3 crystals. *2D Mater.* **7**, 015007 (2019).
26. Sivadas, N., Okamoto, S., Xu, X., Fennie, C. J. & Xiao, D. Stacking-Dependent Magnetism in Bilayer CrI_3. *Nano Lett.* **18**, 7658-7664 (2018).
27. Jiang, P. *et al.* Stacking tunable interlayer magnetism in bilayer CrI_3. *Phys. Rev. B* **99**, 144401 (2019).
28. Soriano, D., Cardoso, C. & Fernández-Rossier, J. Interplay between interlayer exchange and stacking in CrI_3 bilayers. *Solid State Commun.* **299**, 113662 (2019).
29. Cheng, R., Daniels, M. W., Zhu, J. G. & Xiao, D. Antiferromagnetic spin wave field-effect transistor. *Sci. Rep.* **6**, 24223 (2016).
30. Jungwirth, T., Marti, X., Wadley, P. & Wunderlich, J. Antiferromagnetic spintronics. *Nat. Nanotechnol.* **90**, 015005 (2016).
31. Zhang, Y., Chuang, T. H., Zakeri, K. & Kirschner, J. Relaxation time of terahertz magnons excited at ferromagnetic surfaces. *Phys. Rev. Lett.* **109**, 087203 (2012).
32. Qin, H. J., Zakeri, K., Ernst, A. & Kirschner, J. Temperature Dependence of Magnetic Excitations: Terahertz Magnons above the Curie Temperature. *Phys. Rev. Lett.* **118**, 127203 (2017).
33. Qin, H. J. *et al.* Long-living terahertz magnons in ultrathin metallic ferromagnets. *Nat. Commun.* **6**, 6126 (2015).
34. Castellanos-Gomez, A., Buscema, M. & Molenaar, R. Deterministic transfer of two-dimensional materials by all-dry viscoelastic stamping. *2D Mater.* **1**, 011002 (2014).
35. Zhang, X., Li, L., Weber, D. *et al.* Gate-tunable spin waves in antiferromagnetic atomic bilayers. *Nat. Mater.* (2020). https://doi.org/10.1038/s41563-020-0713-9

Acknowledgements: We thank Nathan Wilson for the helpful discussion. This work was mainly supported by the Department of Energy, Basic Energy Sciences, Materials Sciences and Engineering Division (DE-SC0012509). Device fabrication and understanding of magnon optical

selection rules are partially supported by AFOSR MURI 2D MAGIC (FA9550-19-1-0390). Work at ORNL (MAM) was supported by the US Department of Energy, Office of Science, Basic Energy Sciences, Materials Sciences and Engineering Division. K.W. and T.T. acknowledge support from the Elemental Strategy Initiative conducted by the MEXT, Japan and the CREST (JPMJCR15F3), JST. BH acknowledges partial support from NW IMPACT. XX acknowledges the support from the State of Washington funded Clean Energy Institute and from the Boeing Distinguished Professorship in Physics.

Author contributions: XX, JC and BH conceived the experiment. JC and BH fabricated and characterized the samples, assisted by AM and PT. JC and BH performed the Raman and magnetic circular dichroism measurements, assisted by PT and TS. JC, BH, NS, DX, and XX analysed and interpreted the results. TT and KW synthesized the hBN crystals. MAM synthesized and characterized the bulk CrI_3 crystals. JC, BH, XX and DX wrote the paper with input from all authors. All authors discussed the results.

Competing Interests: The authors declare no competing financial interests.

Additional Information: Supplementary information is available in the online version of this paper. Reprints and permission information is available online at http://nature.com/reprints. Correspondence and requests for materials should be addressed to XX or DX.

Figures:

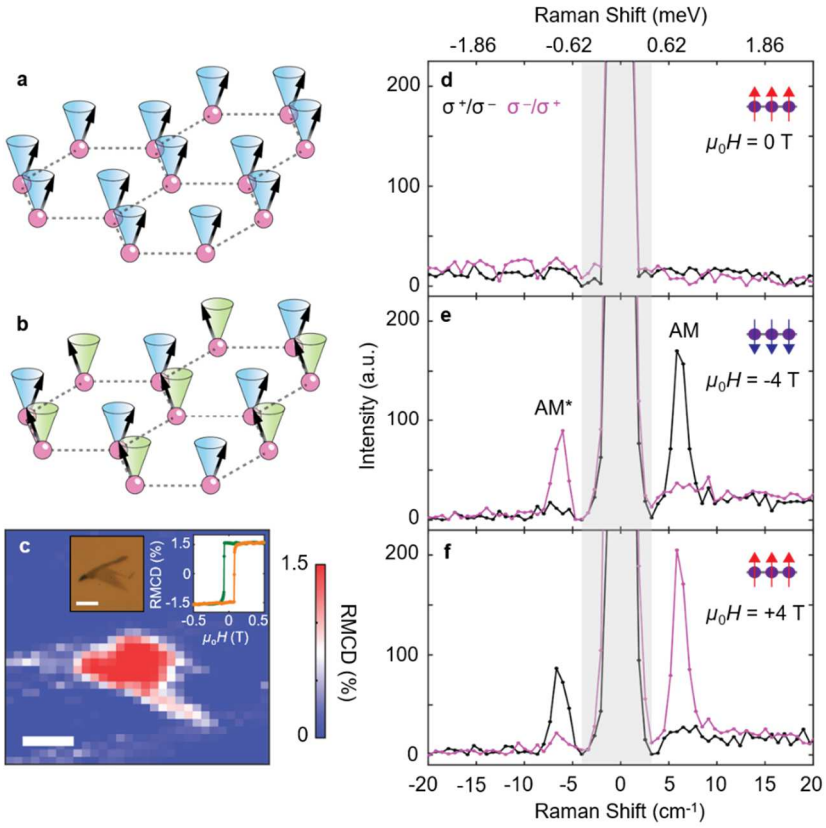

Figure 1 | Spin wave diagram of monolayer CrI_3, sample characterization and low-frequency Raman spectra. a-b, Depiction of the two types of spin waves in ferromagnetic monolayer CrI_3: **a** corresponds to the in-phase acoustic mode while **b** corresponds to the out-of-phase optical one. **c,** Zero-field reflective magnetic circular dichroism (RMCD) map of an encapsulated monolayer CrI_3 flake. Scale bar: 4 µm. The right inset shows an RMCD sweep taken at the center of the flake while the left inset shows an optical micrograph of the sample with a scale bar of 10 µm. **d-f,** Low-frequency cross-polarized Raman spectra taken at **d,** zero-field **e,** -4 T, and **f,** 4 T. The grey box indicates the spectral range of our optical filter below which the magnon is unresolvable.

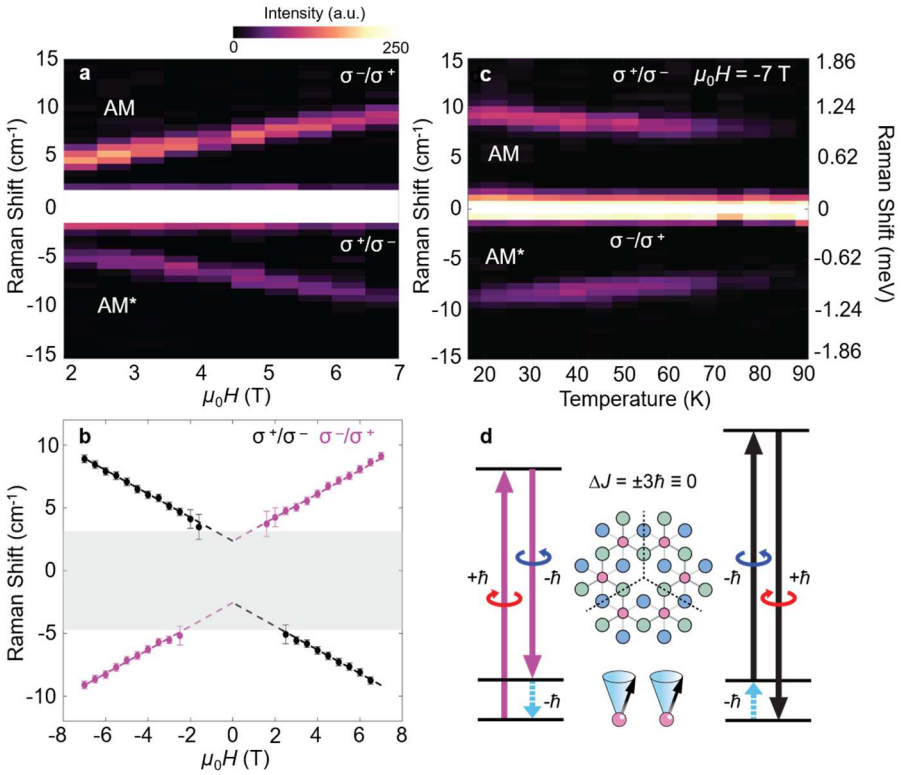

Figure 2 | Magnetic field and temperature-dependence of spin waves in monolayer CrI_3. a, Color map of magnetic field-dependent Raman measurements of monolayer CrI_3 in the field range from 2 to 7 T. Data above 0 cm^{-1} is taken in the σ^-/σ^+ channel while data below 0 cm^{-1} is taken in the σ^+/σ^- channel. **b,** The center of the magnon features obtained by Lorentzian fits of the spectra plotted as a function of field from –7 to 7 T. The dashed line shows the expected Zeeman energy shift for an $S = 1$ quasiparticle with a zero-field energy of 2.4 cm^{-1} (~0.3 meV). The error bars represent the uncertainty of the Lorentzian fit used to determine the peak center. **c,** Color map of temperature-dependent Raman measurements indicate a gradual redshifting with temperature until the scattering vanishes at temperatures above ~80 K. **d,** Optical selection rules of the one-magnon scattering in monolayer CrI_3. The left (right) energy diagram corresponds to Stokes (anti-Stokes) scattering in the spin-up state. The total change in angular momentum of $\pm 3\hbar$ is equivalent to 0 in the honeycomb lattice shown in the middle. Pink, green, and blue circles in the honeycomb lattice represent Cr^{3+}, top I^-, and bottom I^- ions respectively.

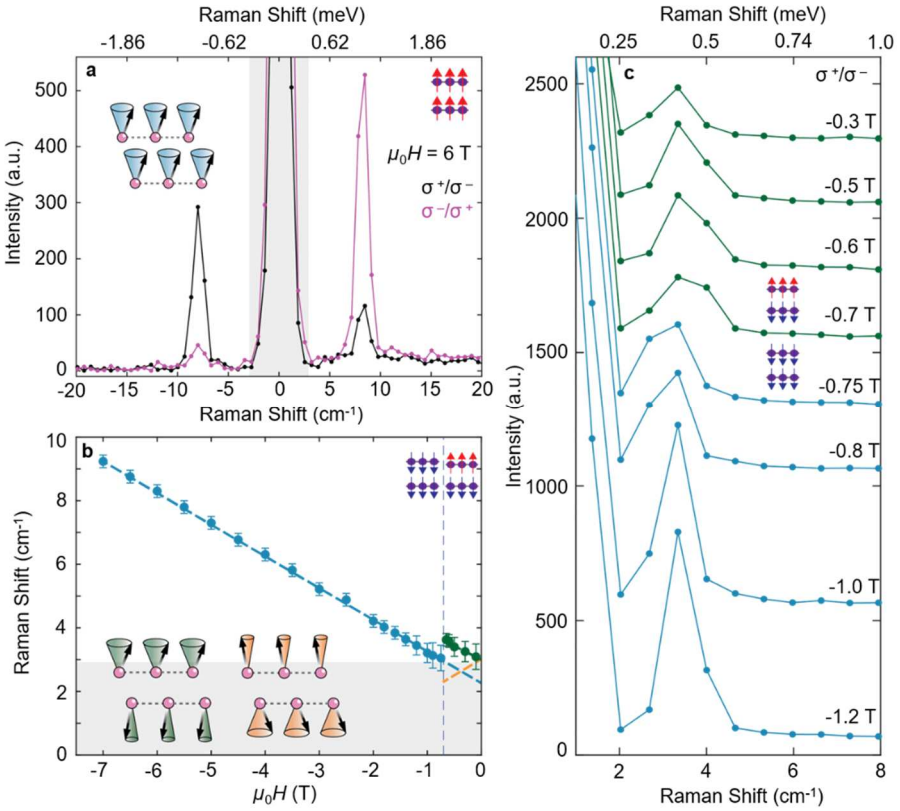

Figure 3 | Magnon scattering in magnetic CrI_3 bilayers. a, Low-frequency Raman spectrum of a CrI_3 bilayer in the spin-up FM-like state at an applied field of 6 T. **b,** The magnon frequency in the field range from -7 T to 0 T. The dashed blue line is a linear fit of the acoustic magnon energy indicating a Zeeman shift of g factor ~ 2.1 and intercept of 2.2 cm^{-1} (0.27 meV). Between -0.7 T and -0.75 T, a metamagnetic transition indicated by the grey dashed line occurs as the bilayer switches to the layered AFM state which should host two magnon modes that shift oppositely with applied field. These two magnon modes are illustrated in the bottom-left inset. The green dashed line plots the mode which blueshifts (left cartoon of inset) and is resolvable in our experiments while the orange dashed line indicates the mode which redshifts (right cartoon of inset) into the spectral filter which is indicated by the grey box. The intercept of the green line indicates that the zero-field AFM magnon energy is ~ 3 cm^{-1} (0.37 meV). The error bars represent the uncertainty of the Lorentzian fit used to determine the magnon energy. **c,** Low-frequency Raman spectra taken as the bilayer goes through the transition with increasing magnetic field strength. The switching of the acoustic magnon modes is evident as the peak centered at ~3.6 cm^{-1} (0.44 meV) at -0.7 T disappears, and a lower energy mode emerges.

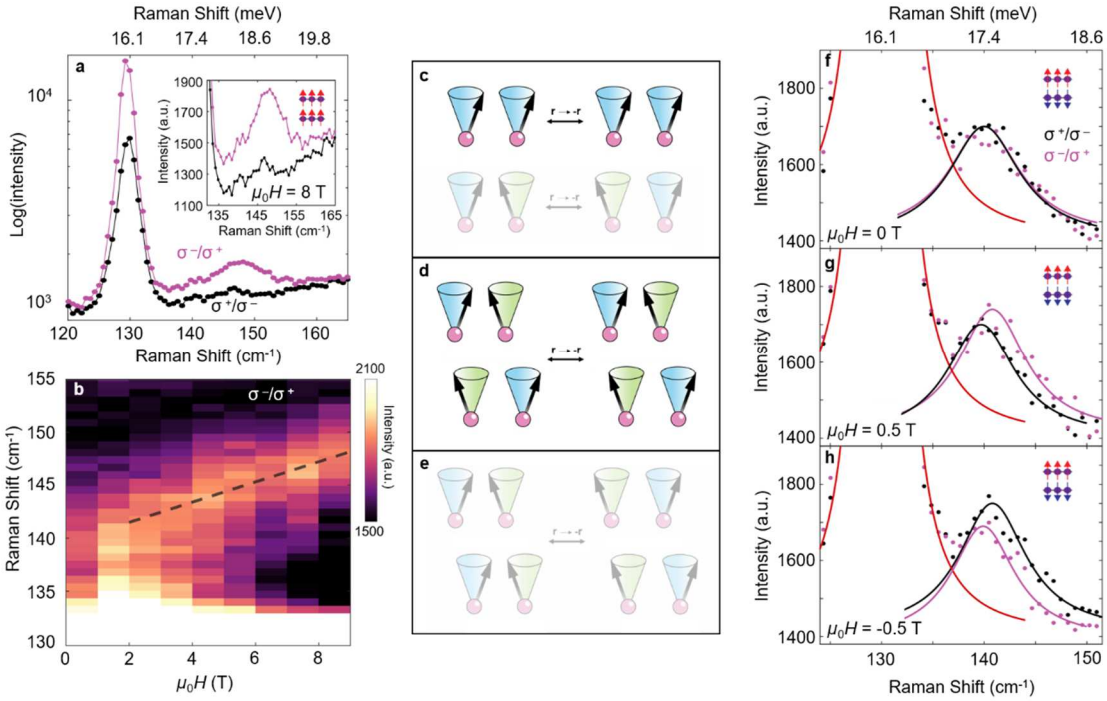

Figure 4 | Optical magnons in bilayer CrI_3. a, Raman scattering from bilayer CrI_3 in an applied field of 8 T with intensity plotted in a log scale. The right inset displays a zoomed in plot of a cross-polarized feature centered at ~148 cm^{-1} (4.4 THz or 18.4 meV). **b,** Field dependence of the optical magnon from 0 T to 9 T. The feature shifts with a g factor ~ 2 (dashed black line), confirming its magnon nature. **c,** Illustration of acoustic and optical magnons in a CrI_3 monolayer unit cell. After applying the inversion operator, **-r**, the acoustic magnon remains invariant while the optical magnon accumulates a π-phase shift in its spin precession. Given that the monolayer is centrosymmetric, the parity-even acoustic magnon is Raman-active while the parity-odd optical magnon is Raman-silent. **d-e,** Cartoons of optical magnons in an FM-like CrI_3 bilayer. Davydov-like splitting of the optical magnon in a monolayer results in **d,** a parity-even, Raman-active mode and **e,** a parity-odd, Raman-silent mode. **f,** Zero-field Raman spectra of bilayer CrI_3. The solid lines are Lorentzian functions plotted as guides-to-the-eye. Contrary to the FM-like state which shows a strong favoring of one scattering channel (e.g. σ^-/σ^+ for **a**), the optical magnon in the zero-field AFM state appears equally in both cross-circular channels. **g,** Upon application of magnetic field, there is a splitting between the two optical magnon modes as the σ^-/σ^+ mode blue-shifts and σ^+/σ^- mode red-shifts. **h,** When the direction of applied field is flipped, the energy shift of the modes is also reversed.

Supplementary information for

Direct observation of 2D magnons in atomically thin CrI_3

Authors: John Cenker[1†], Bevin Huang[1†], Nishchay Suri[2], Pearl Thijssen[1], Aaron Miller[1], Tiancheng Song[1], Takashi Taniguchi[3], Kenji Watanabe[3], Michael A. McGuire[4], Di Xiao[2]*, Xiaodong Xu[1,5]*

[1]Department of Physics, University of Washington, Seattle, Washington 98195, USA
[2]Department of Physics, Carnegie Mellon University, Pittsburgh, Pennsylvania 15213, USA
[3]National Institute for Materials Science, 1-1 Namiki, Tsukuba 305-0044, Japan
[4]Materials Science and Technology Division, Oak Ridge National Laboratory, Oak Ridge, Tennessee 37831, USA
[5]Department of Materials Science and Engineering, University of Washington, Seattle, Washington 98195, USA

[†]These authors contributed equally to this work.

*Corresponding author's e-mail: xuxd@uw.edu; dixiao@cmu.edu

Content:

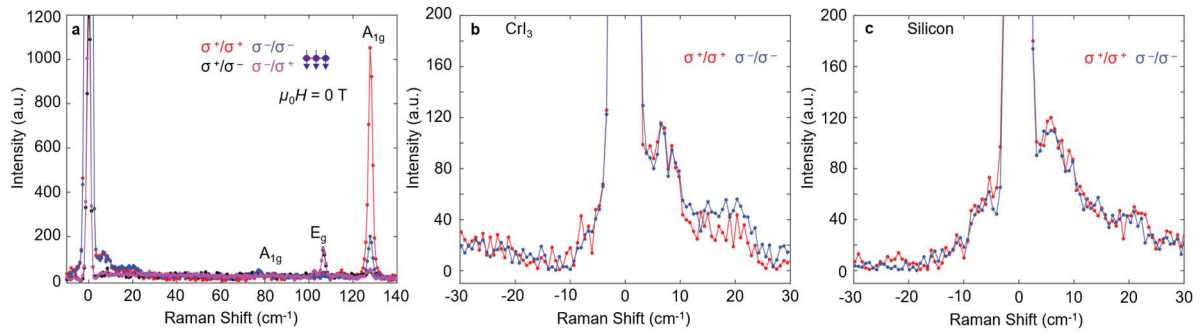

Figure S1 | Monolayer CrI_3 phonon modes and low-frequency co-circularly polarized spectra. a, Zero-field Raman spectra of monolayer CrI_3 showing the standard phonon modes, i.e. A_{1g} phonons at ~127 cm^{-1} and 77 cm^{-1} in the co-circular channels and E_g modes at ~108 cm^{-1} in the cross-circular channel. **b-c,** Low frequency co-circularly polarized Raman scattering on monolayer CrI_3 and SiO_2/Si substrate. The low-frequency scatter originates from quasi-elastic scattering off the substrate given that the low-frequency co-polarized scatter on monolayer (**b**) is the same as that on silicon (**c**).

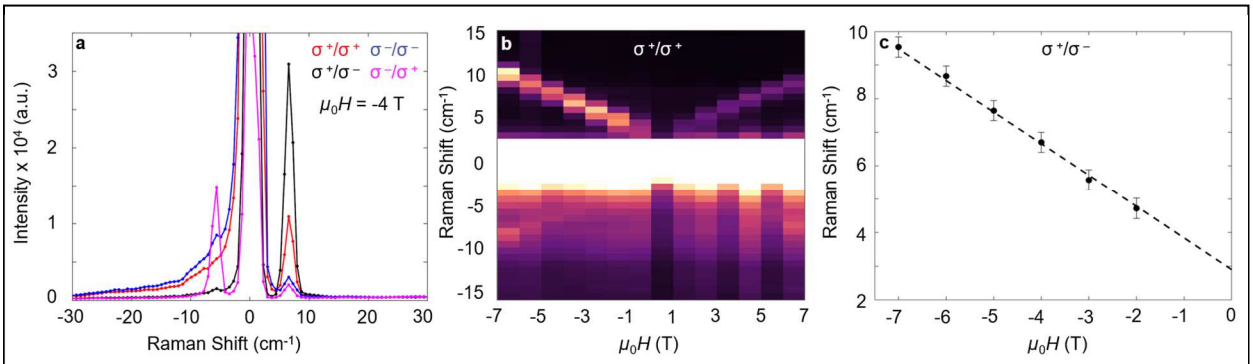

Figure S2 | Acoustic magnon scattering in unexfoliated single crystal CrI_3. a, Low-frequency circularly polarized Raman spectra of bulk single crystal CrI_3. Although the magnon scattering is still predominantly in the cross-circularly polarized channel, a large component appears in the co-circular σ^+/σ^+ channel. **b,** Color map of the magnetic field dependence of σ^+/σ^+ scattering. The linear shift of ~2 μ_B indicates that it arises from magnon scattering and rules out acoustic phonons. **c,** The energy of the acoustic magnon from the σ^+/σ^- channel plotted as a function of magnetic field from -7 to -2 T. The dashed line indicates a Zeeman shift of 2 μ_B with a zero-field energy of ~2.8 cm^{-1} and fits the energy shift of the low-energy peak well. The zero-field energy of the acoustic magnons is determined mainly by the out-of-plane magnetic anisotropy.

Supplementary Note 1 – Cross-comparison of bulk magnon measurements

We note that the bulk FM magnon observed in this work (Fig. S2) has an energy consistent with the results from ref. [1]. However, ref. [1] reports an additional surface AFM magnon mode with a zero-field energy of ~ 4 cm^{-1}, which should be detectable in our experimental setup. The presence of both bulk FM and surface AFM magnon modes indicates the coexistence of magnetic orders with the surface layers being AFM and the bulk being FM[1]. In CrI_3, the interlayer coupling is strongly tied to the stacking order. As a result, thin exfoliated CrI_3 samples maintain monoclinic stacking and AFM interlayer coupling, in contrast to the unexfoliated bulk single crystal which has rhombohedral stacking and FM coupling at low temperatures[2-4]. Consequently, a possible explanation for why ref. [1] observes the surface AFM magnon mode in bulk single crystal and we do not is that the bulk crystal in our work was not exfoliated and thus solely FM, while the samples measured in ref. [1] were freshly cleaved, leading to a surface AFM phase.

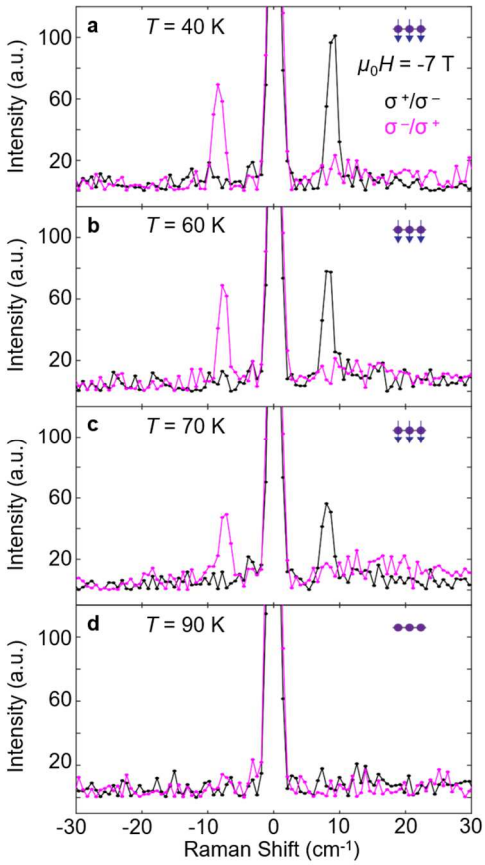

Figure S3 | Low-frequency Raman spectra of monolayer CrI_3 at select temperatures. a-d, Cross-circularly polarized Raman spectra taken at various temperatures in an applied field of -7 T. Due to the applied field, the magnon is shifted away from the Rayleigh line and is present until ~80 K, well above the Curie temperature of T_c ~ 45 K. Notably, the linewidth does not appear to significantly broaden throughout this temperature range.

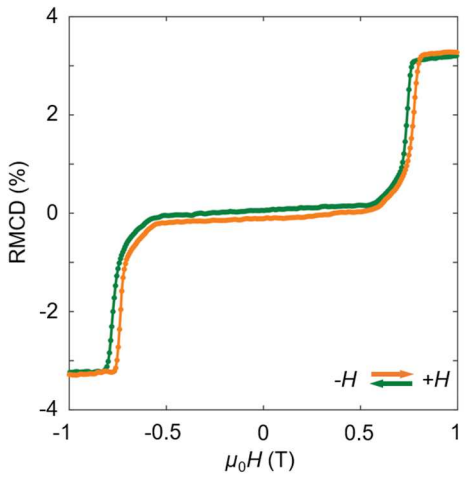

Figure S4 | RMCD measurement of bilayer CrI_3. Field dependent RMCD measurements of the same bilayer CrI_3 flake shown in Fig. 3. The data points in green indicate RMCD measurements taken while the field is swept down while the orange points are taken as the field is swept up. These measurements show the spin-flip transition occurs at around ±0.7 T.

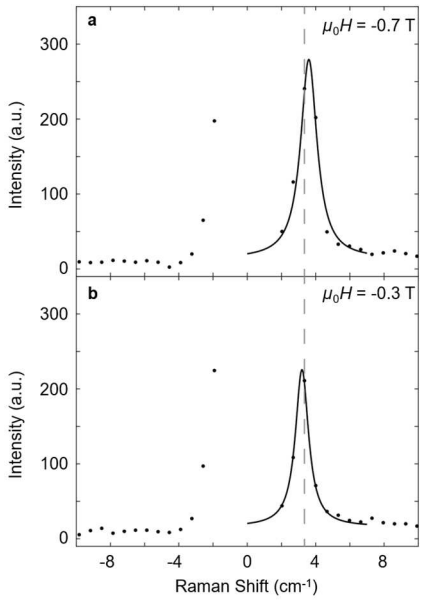

Figure S5 | Lorentzian fits of the acoustic magnon in AFM bilayer CrI_3. Lorentzian fit of the acoustic magnon in bilayer CrI_3 in an applied field of **a,** -0.7 T and **b,** -0.3 T. The center of the Lorentzian fits are at 3.6 cm^{-1} and 3.2 cm^{-1} respectively. The grey dashed line indicates the CCD pixel of the spectrometer with the highest counts of the magnon feature.

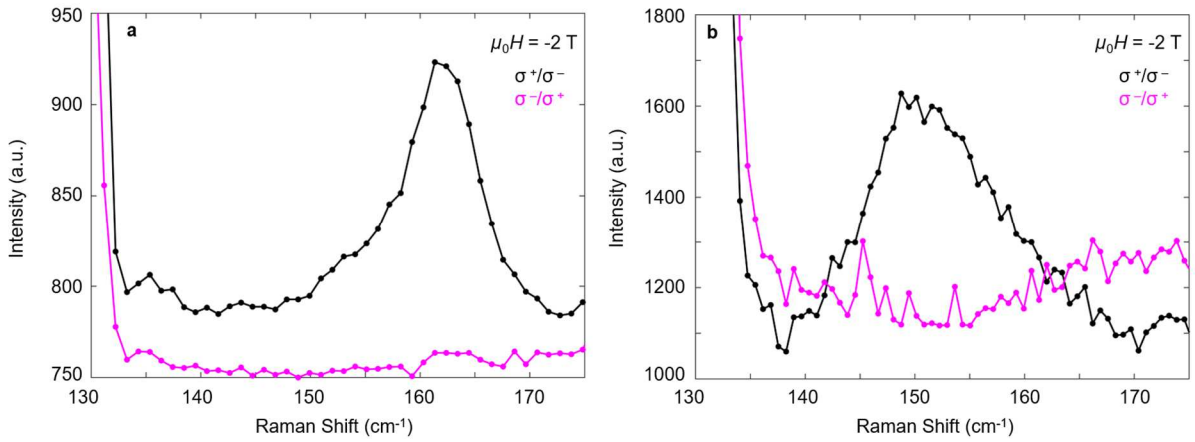

Figure S6 | Optical magnons in bulk CrI_3. a, Cross-circularly polarized scattering channels in exfoliated thin bulk (~100 nm thickness) showing the optical magnon at an applied field of -2 T. In this sample, the magnon appears at a higher frequency than in bilayer with a zero-field energy of ~160 cm^{-1} (4.8 THz). **b,** Optical magnon in unexfoliated single-crystal CrI_3 in an applied field of -2 T. In this thickness, the optical magnon appears at a zero-field frequency of ~148 cm^{-1}.

References:

1. Li, S. *et al.* Magnetic field-induced quantum phase transitions in a van der Waals magnet. *Phys. Rev. X* **10**, 011075 (2020).
2. Ubrig, N. *et al.* Low-temperature monoclinic layer stacking in atomically thin CrI_3 crystals. *2D Mater.* **7**, 015007 (2019).
3. Song, T., *et al*. Switching 2D magnetic states via pressure tuning of layer stacking. *Nat. Mater.* **18,** 1298–1302 (2019).
4. Li, T., *et al.* Pressure-controlled interlayer magnetism in atomically thin CrI_3. *Nat. Mater.* **18,** 1303–1308 (2019).